

Assessment of Scatter Components in High-Resolution PET: Correction by Nonstationary Convolution Subtraction

M. Bentourkia, P. Msaki, J. Cadorette and R. Lecomte

Department of Nuclear Medicine and Radiobiology, University of Sherbrooke, Sherbrooke, Québec, Canada

This paper describes a new approach to determine individual scatter kernels and to use them for scatter correction by integral transformation of the projections. **Methods:** Individual scatter components are fitted on the projections of a line source by monoexponentials. The position-dependent scatter parameters of each scatter component are then used to design non-stationary scatter correction kernels for each point in the projection. These kernels are used in a convolution-subtraction method which consecutively removes object, collimator and detector scatter from projections. This method is based on a model which assumes that image degradation results exclusively from Compton interactions of annihilation photons, thus neglecting further Compton interactions of object scatters with collimator and detector. **Results:** Subtraction of the object scatter component improved contrast typical of what is obtained with standard convolution-subtraction methods. The collimator scatter component is so weak that it can be safely combined with object scatter for correction. Subtraction of detector scatter from images did not improve contrast because statistical accuracy is degraded by removing counts from hot regions while cold regions (background) remain unchanged. **Conclusion:** Subtraction of object and collimator scatter improves contrast only. The slight gain in image sharpness resulting from the subtraction of detector scatter does not justify removal of this component at the expense of sensitivity.

Key Words: PET; scatter components; detector scatter; scatter correction

J Nucl Med 1995; 36:121-130

Scatter is one of the main causes of degradation of PET images, resulting in loss of contrast, resolution and quantitative accuracy. Until recently (1), object and collimator scatters were perceived as being the only scatter components responsible for degradation (2-7). However, in addition to the object and collimator scatter, photon spillage from primary to secondary detectors can add a significant scatter contribution to the events acquired with very high

resolution PET systems based on arrays of narrow and deep detectors (8-13). In these systems, detector scatter tends to reduce the overall spatial resolution, mainly by broadening the distribution below the FWTM (11,12). Correction for these effects requires knowledge of the magnitude and shape of individual scatter components as a function of source position, scattering medium and energy threshold.

In this work, a method is presented to extract the scatter components originating from the object, the collimator and the detector by fitting the projection response functions obtained with a line source at different locations in the FOV with simple analytical functions. The amplitude and shape of the individual scatter response functions are shown to be well described by monoexponential functions which can then be used to generate nonstationary scatter correction kernels. These kernels are subsequently used for removal of the individual scatter components in images by a consecutive convolution-subtraction approach based on the integral transform method (3).

THEORY

Scatter Components

The measured projection P_m of a high-resolution PET system can be treated as the sum of true events (T), object (S_o), collimator (S_c) and detector (S_d) scattered events:

$$P_m = T + S_o + S_c + S_d. \quad \text{Eq. 1}$$

The scatter components in this model are assumed to be the result of independent processes which neglect subsequent Compton interactions of object scattered photons in the collimator and detector, as well as subsequent Compton interactions of collimator scattered photons in the detector. This is a valid assumption when such processes are weak or have negligible effects on the scatter distribution (6).

Many scatter correction methods estimate the scatter response function of the system from the response to a line or point source (2-6, 14-16). Based on the above assumption, the normalized overall system response $h(x_s, x)$ to a line source at location in the object corresponding to position x_s in the projection is also given as the sum of four components:

Received Dec. 23, 1993; revision accepted July 12, 1994.
For correspondence or reprints contact: Dr. Roger Lecomte, Department of Nuclear Medicine and Radiobiology, Université de Sherbrooke, Sherbrooke, Québec, Canada J1H 5N4.

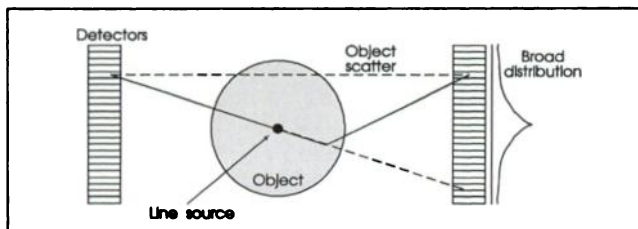


FIGURE 1. Schematic diagram of the origin and shape of object scatter.

$$h(x_s, x) = \sum_i h_i(x_s, x), \quad \text{Eq. 2}$$

where $h_i(x_s, x)$ are the individual position-dependent projection response functions for object scatter ($i = o$), collimator scatter ($i = c$), detector scatter ($i = d$) and intrinsic or geometric detector response ($i = g$). Their relative intensities are described by the scaling factors f_i which represent the fraction of each component ($\sum f_i = 1$):

$$f_i(x_s) = \int h_i(x_s, x) dx. \quad \text{Eq. 3}$$

It follows from the above assumptions that the collimator and detector scatter components can be estimated from a measurement made with the line source in the absence of the scattering media, since the physical processes leading to these components are independent of the object. The dependence of $h(x_s, x)$ on source depth in the object is weak, as many authors have demonstrated (2-4). The depth dependence of the object scatter component was thus assumed negligible in this work.

Object Scatter. The object scatter component is formed by annihilation photons which have interacted in the object by Compton effect. Figure 1 is a schematic representation of a single-interaction object scatter. The object scatter profile in the projection must be estimated for every object since it is dependent upon the size, shape and uniformity of the media around the source. Since the attenuation path lengths about the source located at the center of a uniform cylindrical object are symmetrically distributed, the object scatter distribution is expected to be symmetric about $x_s = 0$. The asymmetry of the distribution progressively increases as the source moves laterally towards the edge of the object. The outer wing has a lower slope because it corresponds to the side with smaller photon path lengths in the object (2-5,17). The amplitude of object scatter is also expected to decrease across the FOV due to the same effect.

Collimator Scatter. Figure 2 is a schematic representation of the origin of the collimator scatter in the projection. Based on the assumption of independent processes, this scatter component can be estimated from the measurement of a line or point source in air. Scattering in the collimator takes place closer to the detector and is forward peaked. The corresponding projection is thus expected to be centered on the source position and slightly narrower than the

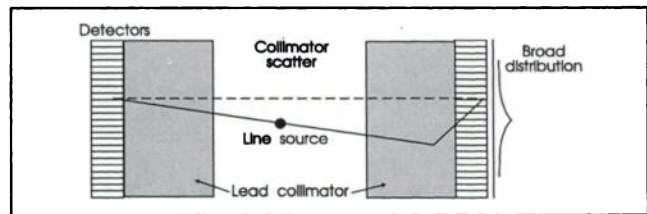


FIGURE 2. Schematic diagram of the origin and shape of collimator scatter.

object scatter. The collimator scatter distribution is characteristic of the system configuration. For suitably designed collimators, the solid angle for coincident radiation incident from the source is relatively small and, therefore, this scatter component is expected to be small (2). In practice the collimator scatter component is mixed with, but indistinguishable from, other effects such as single gamma events detected in coincidence with annihilation radiation.

Detector Scatter. High resolution PET systems are often made with long narrow detectors to increase detection efficiency and spatial resolution. However, the narrower the detectors, the greater the spillage of annihilation photons from primary to secondary detectors in the array (10,13). Case 4 in Figure 3 illustrates the effect of annihilation photon spillage where a small amount of energy below lower discrimination level is deposited in the primary detector and the rest is deposited and registered in a secondary detector. Annihilation photons scattered by surrounding materials such as intercrystal shielding septa or detector package and registered in a neighboring detector also contribute to detector scatter. Due to the high density of detector materials, this scatter contribution is confined to a narrow distribution around the primary detector, as shown in Figure 4. For this reason, the contribution from detector scatter has been ignored in medium- and low-resolution scanners, as it has a negligible effect on the overall response function. For the same reason, it has been assumed in this work that scattering in the detector has a negligible effect on the object and collimator scatter distributions. The detector scatter is characteristic of the detec-

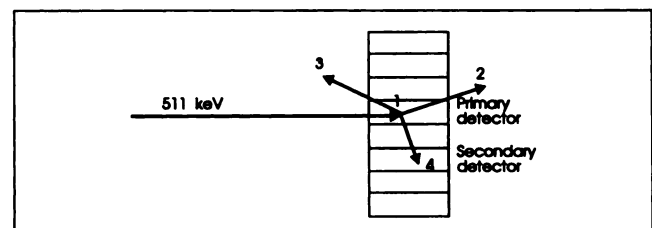


FIGURE 3. Illustration of detector interaction schemes: (Case 1) photoelectric interaction depositing all the incident energy in the primary detector; (Case 2) Compton forward scatter depositing a small amount of energy ($E \leq 250$ keV) in the primary detector; (Case 3) Compton backward scatter depositing a larger amount of energy ($250 \text{ keV} \leq E \leq 340$ keV) in the primary detector; and (Case 4) multiple-energy deposit in primary and secondary detectors.

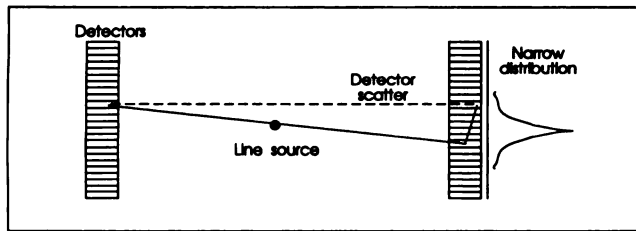


FIGURE 4. Schematic diagram of the origin and shape of detector scatter.

tion system and is dependent upon the energy discrimination threshold (12).

Geometric Detector Response Function. The geometric detector response function is formed by annihilation photons which have not interacted with neither the object nor the collimator. Since such photons carry exact information about the location of the source and the concentration of radioactivity in the object, they form the true component. According to Figure 3, annihilation photons impinging on the detector array can be completely absorbed in the primary crystal (Case 1), be scattered in the primary crystal and either escape from the detector array (Cases 2 and 3) or be absorbed in a secondary crystal (Case 4). When the energy deposited in the primary crystal is above the lower discrimination threshold, Cases 1, 2 and 3 contribute to the geometric detector response.

The events associated with Case 4 become ambiguous, and are thereby rejected when energies deposited in secondary and primary crystals are both greater than the lower energy discrimination levels of respective detectors. If the energy deposited in the primary detector is above the energy discrimination level and the scattered energy deposited in the secondary detector is below the energy discrimination level or lost in the intercrystal septa or detector package, the event becomes part of the geometric detector response, which is well-positioned. Monte Carlo simulations of annihilation photons impinging on a linear array of $3 \times 5 \times 20$ mm BGO crystals without package have shown that the relative amounts of events illustrated in Figure 3 are: 64% for Case 1, 23% for Cases 2 and 3 combined and 13% for Case 4 (1).

When the line-of-response (LOR) passes through the center of the tomograph FOV, the detectors are parallel and the geometric detector response function, which is dictated exclusively by the physical dimensions of the detectors and is triangular in shape, as shown in Figure 5 (left). As the source is moved off center, detector overlap increases and, as a result, the shape of the geometric detector response function varies with source position in the FOV. Once the source position has been specified, the width of the geometric detector response function is uniquely defined by a set of parallel LORs connecting the coincident detectors over the source. Note that other effects, including positron range in the source and deviation from 180° emission of the annihilation photons, which broaden the distribution by amounts comparable to the

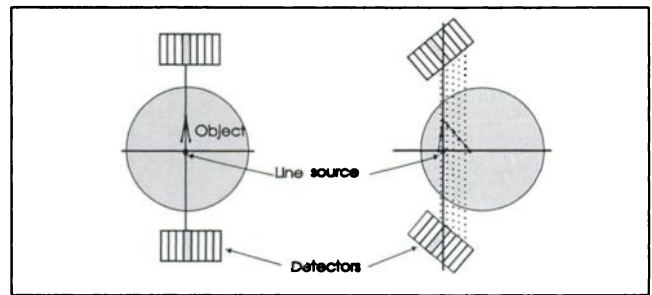


FIGURE 5. Geometric detector response function for LORs crossing the center (left) and off-center (right). Note that the extent of the geometric detector response is entirely determined by the geometry of the detectors.

detector geometric and scatter components, will be considered to be part of the detector scatter component with the current assumptions (18).

Consecutive Convolution-Subtraction Approach

Bergström et al. (3) have shown that the scatter distribution in the projection can be estimated and subtracted by integral transformation of the projections using a scatter correction kernel. Since the object, collimator and detector scatter components were assumed to be independent of each other, the desired or corrected projection data P_{ocd} consisting of only true events can be estimated from the measured projection data P_m by successive convolution (*) subtraction processes of the form:

$$P_o = P_m - P_m * F_o$$

$$P_{oc} = P_o - P_o * F'_c \quad \text{Eq. 4}$$

$$P_{ocd} = P_{oc} - P_{oc} * F''_d,$$

where P_i is the projection free of scatter component(s) $i = o, oc, ocd$. F_o , F'_c and F''_d are the scatter correction kernels for object, collimator and detector scatter, respectively, estimated from line source measurements as described below. The standard Bergström approach is applied to estimate object scatter from the measured projection P_m . Since the object scatter corrected projection P_o is a better estimate of the trues than P_m , the former is used to estimate the collimator scatter, and so on for the detector scatter. In these calculations, the collimator F_c and detector F_d scatter kernels are renormalized as:

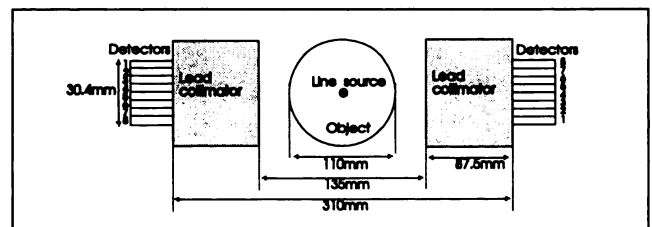


FIGURE 6. Schematic of the PET simulator used for the measurements. One detector array and the object can be rotated to acquire tomographic data.

$$F'_c = \frac{F_c}{1 - f_o} \text{ and } F''_d = \frac{F_d}{1 - f_o - f_c}, \quad \text{Eq. 5}$$

where the fractions f_i are defined in Equation 3. Rearranging Equation 4, the following expression is obtained:

$$P_{\text{ocd}} = \{[P_m * (\delta - F_o)] * (\delta - F'_c)\} * (\delta - F''_d), \quad \text{Eq. 6}$$

where δ is the Dirac delta function as formally defined. Even though the convolution operation is commutative, the order in which the successive convolution-subtraction operations are applied in Equation 6 is not, since it follows from the model used to describe the scatter degradation processes. The innermost convolution removes the overall object scatter from P_m to produce the projection distribution which would result if only annihilation photons were impinging on the detection system. Similarly, the second convolution removes collimator scatter to produce the projection distribution resulting from a pure annihilation photon flux on the detector arrays.

MATERIALS AND METHODS

Phantom Measurements

All measurements were carried out using the Sherbrooke PET camera simulator represented schematically in Figure 6 (11,19). The system was set up to simulate an animal-size, 310-mm diameter ring PET camera with 256 discrete detectors based on avalanche photodiodes (20,21). The energy threshold on each detector was set at 350 keV. The system response functions were measured using a line source of ^{22}Na having an effective diameter of 0.85 mm. Other measurements were made with phantoms containing sources of ^{22}Na in water solutions.

Two sets of measurements were conducted in order to obtain the projection response function $h(x_s, x)$ as a function of position x_s . In the first set, the line source was placed at 11 positions equally spaced from -50 mm to 50 mm along the diameter of the FOV and data forming the parallel projections were acquired. Since projections have 64 bins, it would be necessary to interpolate or take additional measurements along the diameter to obtain the projection response for each bin. In order to overcome this inconvenience, the second set consisted of one tomographic measurement made with a line source at 50 mm from the center. Assuming the response functions are depth independent (2-4), it is conceivable that the projection response function for each bin can be extracted from the sinogram of this single measurement. Both measurements were made with the line source in air and in a 110-mm cylindrical plexiglas phantom.

Additional measurements were made with a cold spot phantom having two 10-mm cylindrical cold regions for contrast evaluation and a pie hot spot phantom having active regions ranging from 1 to 3 mm in diameter for resolution study.

Efficiency calibration measurements were made with a plane source in air after each set of measurements. Randoms were simultaneously acquired in a delayed coincidence time window for all measurements, including the calibration. The data were rebinned into 128 projections of 64 parallel LORs after random subtraction and detector efficiency normalization, as described elsewhere (19). The corrected projections of the line source measurements were used to fit the scatter components. Phantom images were reconstructed by filtered backprojection using projection data interpolated to 0.95 mm bins and with a ramp having

a high frequency roll-off given by a Butterworth filter of parameter $n = 2$ and $f_c = 32 \text{ bin}^{-1}$, unless otherwise specified. No attenuation correction was made in order to assess the effect of scatter correction alone.

Fitting Procedure

In addition to the geometric detector response, the projections are assumed to consist of collimator and detector scatter components for the measurements taken with the line source in air, and of object, collimator and detector scatter components for the measurements taken with the line source in the cylindrical phantom. In this work, only the spatial extent of the simulated geometric detector response was used in the scatter component fitting procedures. The experimental detector response adjusted for this spatial extent is simply the residual after all the scatter components have been subtracted from the measured system response function $h(x_s, x)$.

The scatter functions $h_i(x_s, x)$ were fitted on the measured system response to a line source (corrected as described) by monoexponential functions of the form:

$$\begin{aligned} h_i(x_s, x) &= A_i(x_s)e^{-S_{il}(x_s)|x - x_s|} & x < x_s \\ &= A_i(x_s)e^{-S_{ir}(x_s)|x - x_s|} & x \geq x_s, \end{aligned} \quad \text{Eq. 7}$$

where A_i is the amplitude and S_{il} and S_{ir} are the left and right decay constants or slopes of the position-dependent scatter component $h_i(x_s, x)$, respectively. For each scatter component, the two exponential functions extrapolated from the wings were assumed to have an intersection at the peak position of the measured distribution. The grid-search method of least squares described elsewhere (22) was used to fit the three parameters A_i , S_{il} and S_{ir} of each scatter component. The data in the extreme bins of the projection were excluded to avoid edge effects. The parameters describing the shapes of the collimator scatter components were evaluated from the measurements of the line source in air. These values were used to fix the collimator scatter contributions while fitting the object and detector scatter component in the measurements made with the line source in plastic.

Scatter Correction Kernels

In principle, the desired nonstationary scatter correction kernels required in Equation 6 can be estimated directly for each bin using the line source fitting technique described above. However, this approach is not feasible because of the inevitable large statistical fluctuations of the measured scatter parameters. This difficulty was overcome by approximating the position-dependent scatter parameters by simple analytical functions described below. These functions were used to extrapolate missing data near the edges of the FOV and to generate the desired kernels F_i for each bin in the projection according to:

$$\begin{aligned} F_i(x_s, x) &= \bar{A}_i(x_s)e^{-\bar{S}_{il}(x_s)|x - x_s|} & x < x_s \\ &= \bar{A}_i(x_s)e^{-\bar{S}_{ir}(x_s)|x - x_s|} & x \geq x_s, \end{aligned} \quad \text{Eq. 8}$$

where the amplitude \bar{A}_i and the slopes \bar{S}_{il} and \bar{S}_{ir} are read directly from the analytical functions approximating the scatter parameters. These kernels were used to consecutively subtract the different types of scatter from the measured projection data as described by Equation 6.

Analytical Approximation of Scatter Parameters

Since the intensity of scatter in any material is expected to increase with photon path length, the amplitude of the scatter functions can be approximated by an attenuation law of the form:

$$\bar{A}_i(x_s) = a_{i1} (1 - e^{-a_{i2}d_i(x_s)}), \quad \text{Eq. 9}$$

where a_{i1} and a_{i2} are coefficients to be evaluated from the fit to the experimental values of $\bar{A}_i(x_s)$. The variable $d_i(x_s)$ is the path length of the photons within the object, collimator or detector array for a source at location x_s in the FOV. For the object, $d_o(x_s) = \sqrt{r^2 - x_s^2}$, where r is the radius of the object. In the case of the collimator and detector components, $d_i(x_s)$ is given by $d_i(x_s) = \sqrt{(R_i + L_i)^2 - x_s^2} - \sqrt{R_i^2 - x_s^2}$, where R_i is the internal radius and L_i is the radial length of the collimator or detector.

The left and right slopes of the scatter functions were fitted with exponential functions of the form:

$$\bar{S}_i(x_s) = b_{i1} - b_{i2}e^{-b_{i3}x_s}, \quad \text{Eq. 10}$$

where b_{i1} , b_{i2} and b_{i3} are coefficients to be determined from the fit to the experimental values of $\bar{S}_i(x_s)$. Due to the symmetry of the ring geometry, the values of the left and right slopes of each scatter component are expected to be symmetric about the center. For this reason, respective fits to the experimental $\bar{S}_{ii}(x_s)$ and $\bar{S}_{ii}(x_s)$ for $i = o, c, d$, were constrained to be symmetrical about the center.

Performance Assessment

The performance of the scatter correction procedure was assessed from the images of the cold spot and pie hot spot phantoms where the object, collimator and detector scatter components were successively subtracted. The image contrast for the cold spot images was evaluated using the equation:

$$C = \frac{HR - CR}{HR + CR}, \quad \text{Eq. 11}$$

where HR and CR are counts from hot and cold regions, respectively. Resolution recovery was assessed by visual inspection of the hot spot images and by quantitative measure of the resolution of the line source response functions before and after successive removal of the scatter components.

RESULTS AND DISCUSSION

Scatter Component Fitting

The projection response functions measured with the line source at the center of the FOV in air and in the cylindrical phantom are compared in Figure 7. As expected, the object and collimator scatter contributions are described fairly well by monoexponentials having low slope values. The detector scatter is a narrow distribution confined to the vicinity of the source location in the FOV. Its intensity and shape remain nearly the same irrespective of whether the measurement is made in air or in the phantom. This implies that, in the present imaging situation, this component can be evaluated with adequate accuracy from measurements taken with the source in air or in scattering medium. However, for larger objects, accurate extraction of the detector scatter component may be difficult since it is partly masked by object scatter. In such cases, this component should be estimated from measurements made

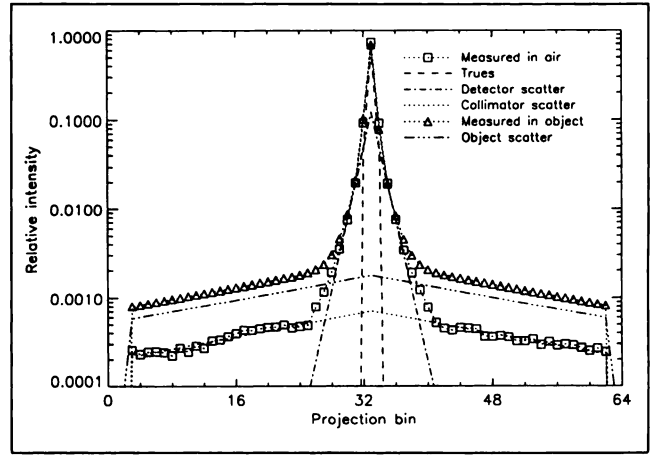


FIGURE 7. Comparison of the response functions, summed over all projections and normalized to the maximum amplitude, for a line source at the center of the FOV in air and in an 11-cm diameter cylindrical phantom. The fitted components are also shown. The detector scatter component is the same for both the measurements in air and in the scattering medium, as expected.

in air. The component representing the trues is the narrowest and its width relates to the system spatial resolution. The ultimate goal of the consecutive convolution-subtraction described in this work is to ensure that images are formed by this component only.

Figure 8 is an example of an off-center ($x_s = 32$ mm) response function measured in the cylindrical phantom. This response function was extracted from the sinogram of a line source located at 50 mm from the FOV center. It is evident that suitable data to estimate the scatter responses as a function of position can be obtained from the tomographic measurement. However, some projections taken from the sinogram are distorted when the source lies outside the channels defined by the sensitive volume of the detectors. It was observed that this sampling effect, which

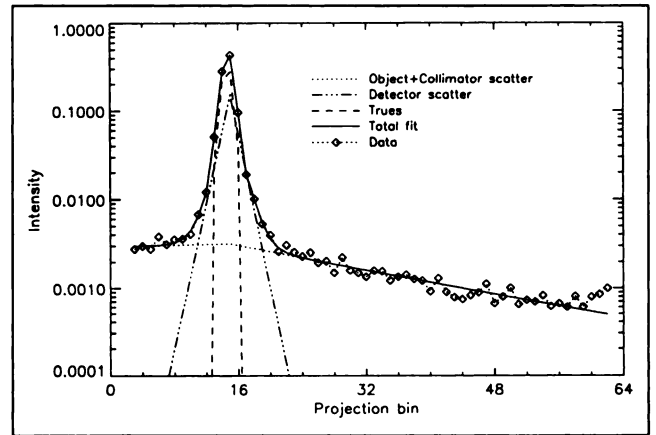


FIGURE 8. Projection extracted from the sinogram of a line source located at 50 mm from the center of the cylindrical phantom. The source position on the projection is 32 mm from the center. The object + collimator and detector fitted components as well as the residual geometric detector response function are shown.

FIGURE 9. Parameters of the object scatter component as a function of position: (A) amplitude and (B) slopes. The analytical approximations to the experimental values are also shown.

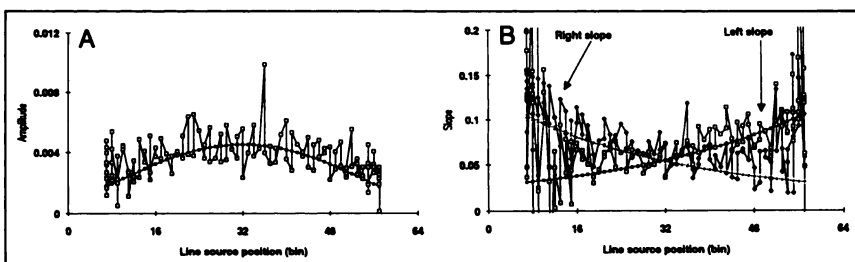
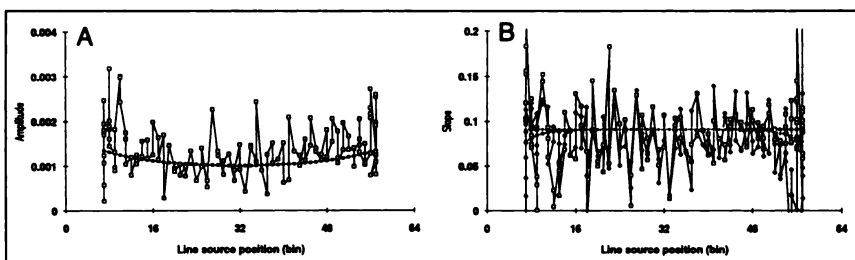


FIGURE 10. Parameters of the collimator scatter component as a function of position: (A) amplitude and (B) slopes. The parameters were obtained from line source response functions in air. The analytical approximations to the experimental values are also shown.



is typical of the high intrinsic resolution and poor packing fraction of the photodiode detectors used in the study (12), does not significantly affect the fitting procedure. The asymmetry is evident from the fits of the object and detector scatter components at 32 mm from the center. It is interesting to note that the steepest slope of the object scatter is on the inner side of the distribution while that of the detector scatter is on the outer side. These observations emphasize the need for selective scatter correction kernels to process the object and detector scatter components by the convolution-subtraction method.

Scatter Parameters

The results of the fitting procedure are summarized in Figures 9–12 where the scatter parameters (amplitude, left

and right slopes, scatter fraction) for each scatter component have been plotted as a function of position in the projection. The analytical functions used to approximate these parameters are also shown and their coefficients are summarized in Table 1.

Figure 9A shows the variation of the object scatter amplitude as a function of source position in the projection data. The highest amplitude is attained at the center of the phantom and its value decreases with distance from the center in accordance with the shape of the cylindrical phantom. This is also reflected by the object scatter fraction shown in Figure 12. Figure 9B represents the left and right slopes of the object scatter response as a function of position. As the source is moved off-center, the slope of

FIGURE 11. Parameters of the detector scatter component as a function of position as obtained from the measurement of the line source in air: (A) amplitude and (B) slopes. The analytical approximations to the experimental values are also shown.

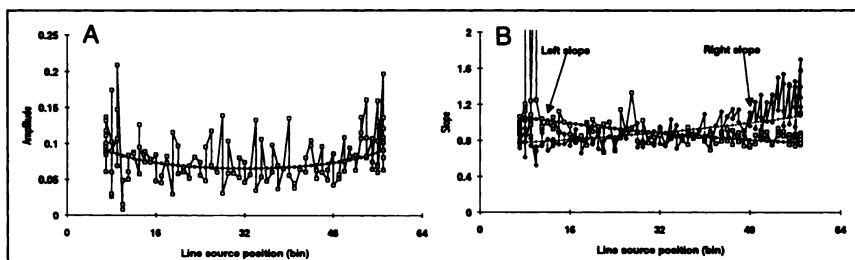


FIGURE 12. True and scatter-to-total fractions for the line source in the cylindrical phantom: (A) experimental values and (B) calculated from analytical approximations.

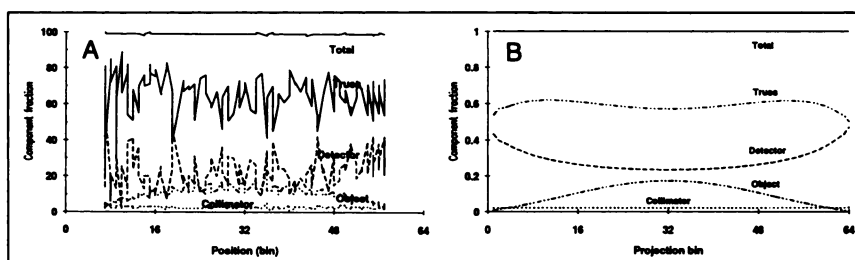


TABLE 1
Coefficients of the Analytical Functions Used to Approximate the Parameters of Object, Collimator and Detector Scatter Functions

	Amplitudes		Slopes*		
	a_1	a_2 (bin ⁻¹)	b_1 (bin ⁻¹)	b_2 (bin ⁻¹)	b_3 (bin ⁻¹)
Object	$9.83 \cdot 10^{-6}$	-0.297	0.1	-0.2	0.06
Collimator	$4.46 \cdot 10^{-5}$	-0.31	$8.0 \cdot 10^{-2}$	0.204	-0.20
Detector	$8.9 \cdot 10^{-3}$	-1.0	0.9	0.19	-0.06

*Coefficients are given for the left slopes. The right slopes can be obtained by symmetry.

the outer wings is observed to decrease while that of the inner wings increases. Independent fits of the analytical function (Eq. 10) to the left and right slope values confirmed the symmetry of the slopes relative to the center with intersecting values at the center (bin 32), in support of the symmetry constrained fitting procedure which was used.

The amplitude of the collimator scatter function varies only slightly with the source position (Fig. 10A) and the slopes are equal and almost constant, except near the edges of the field (Fig. 10B). Although the object and the collimator scatter components appear to have similar shapes for a given source location (see Fig. 7), their scatter parameters as a function of source position are definitely different.

The amplitude and slopes of the detector scatter function are shown in Figure 11A and 11B. As for the collimator, the amplitude of the detector scatter function has a relatively small variation with source position, but the detector scatter fraction increases significantly as the source is moved off center (Fig. 12). This is caused by longer photon path length through the detector array due to inclined photon incidence. Note that the shielding from neighbouring crystals and detector packages both tend to increase detector scatter. The asymmetry of the wings at positions other than the center is attributed to the slightly larger range of forward scattered Compton photons on the inner as compared to the outer side of the ring. This is illustrated schematically in Figure 13. As a result, the inner wing of the detector scatter function has a lower slope (larger extent), contrary to what was observed with the object scatter function.

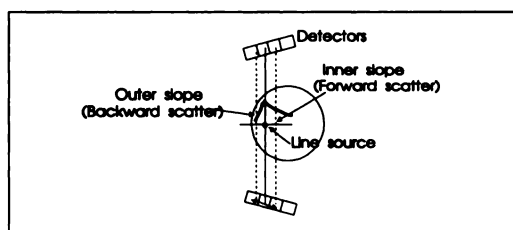


FIGURE 13. Illustration of the origin of asymmetry of the slopes for the detector scatter function. The forward scattered Compton photons have a higher probability to be registered on the inner side of the ring.

Scatter Correction Kernels

We noted from the results presented in Figures 9–12 that the object, collimator and detector scatter components have characteristics which differ significantly not only in magnitude and shape, but also as a function of position in the FOV. The magnitude of the object scatter is particularly large at the center of FOV while the opposite is true for the detector scatter. This means that stationary kernels extracted from a single-line source measurement at the center of FOV would overestimate object scatter and underestimate detector scatter off center. In addition, object and detector scatters show opposite asymmetry characteristics as a function of position in the projection. Independent, nonstationary scatter correction kernels are obviously required for accurate compensation of these two scatter components.

According to Figure 12, the magnitude of object scatter is less than that of the detector scatter for the phantom size used in this study (diameter = 110 mm). Since detector and object scatter distributions are independent, it is evident that as the object size increases, the object scatter is bound to exceed the detector scatter. Under these conditions, it may not be possible to assume that object and detector scattering are independent processes as we have done in this work, since the contribution of object scatter to the detector response may not be negligible. In order to take such effects into consideration and to design appropriate kernels to correct for these contributions, a more sophisticated degradation model would be required.

Scatter Correction

Image Contrast. Figure 14A shows the image of the cold spot phantom uncorrected and successively corrected for object, collimator and detector scatter. As expected, subtraction of the collimator scatter component does not introduce noticeable visual changes in the image. However, subtraction of object and detector scatter introduces significant visual changes in the corrected images. Quantita-

TABLE 2
Contrast of the Cold Spot Phantom Images

	Uncorrected	Object	Collimator	Detector
Contrast	78.6%	93.6%	96.4%	96.5%

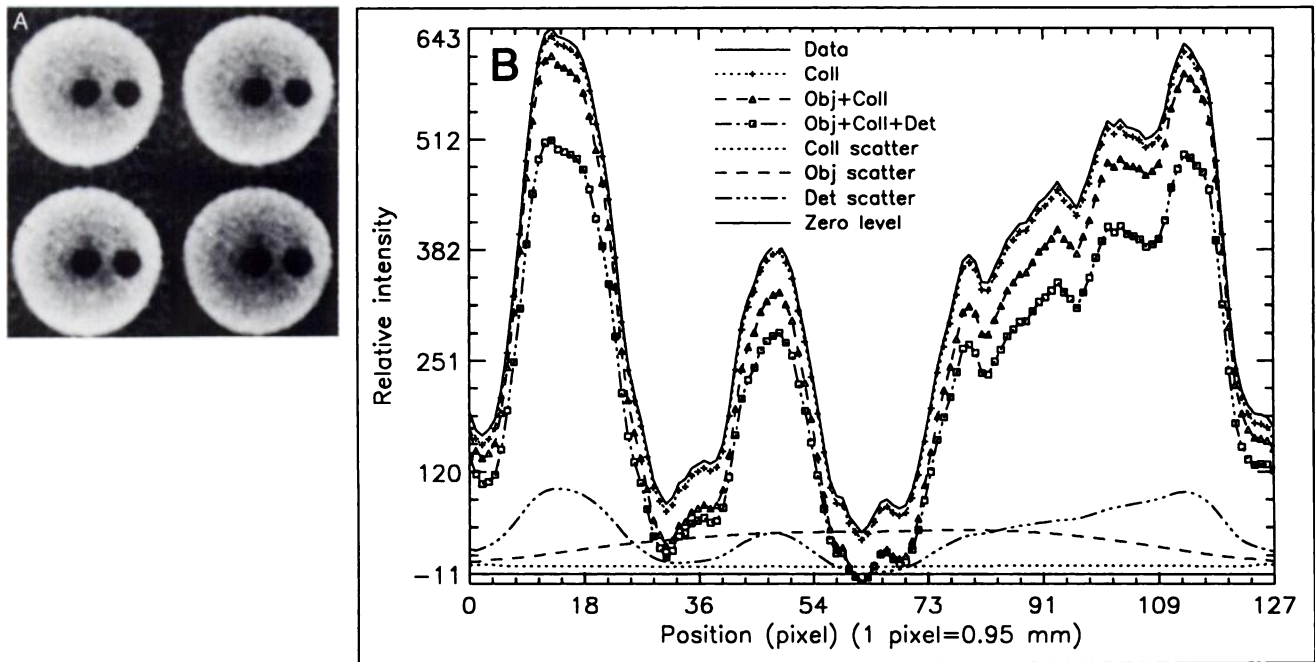


FIGURE 14. (A) Image of the cold spot phantom. Clockwise: without correction; object scatter subtracted; object and collimator scatter subtracted; object, collimator and detector scatter subtracted. (B) Profiles through the cold spots showing the scatter contributions and the resultant profiles after the successive corrections.

tive explanation for these observations can be deduced from the profiles of the corrected images displayed in Figure 14B. The scatter-to-total ratios for the object, collimator and detector are 10%, 2% and 24%, respectively. It is important to note that these amounts will change as the

object size increases or decreases. In a larger object, scattering in the object will reduce photon transmission per unit radioactivity, thereby lowering the true as well as collimator and detector scattered events. The scatter-to-trues ratio, however, is expected to remain unchanged for the

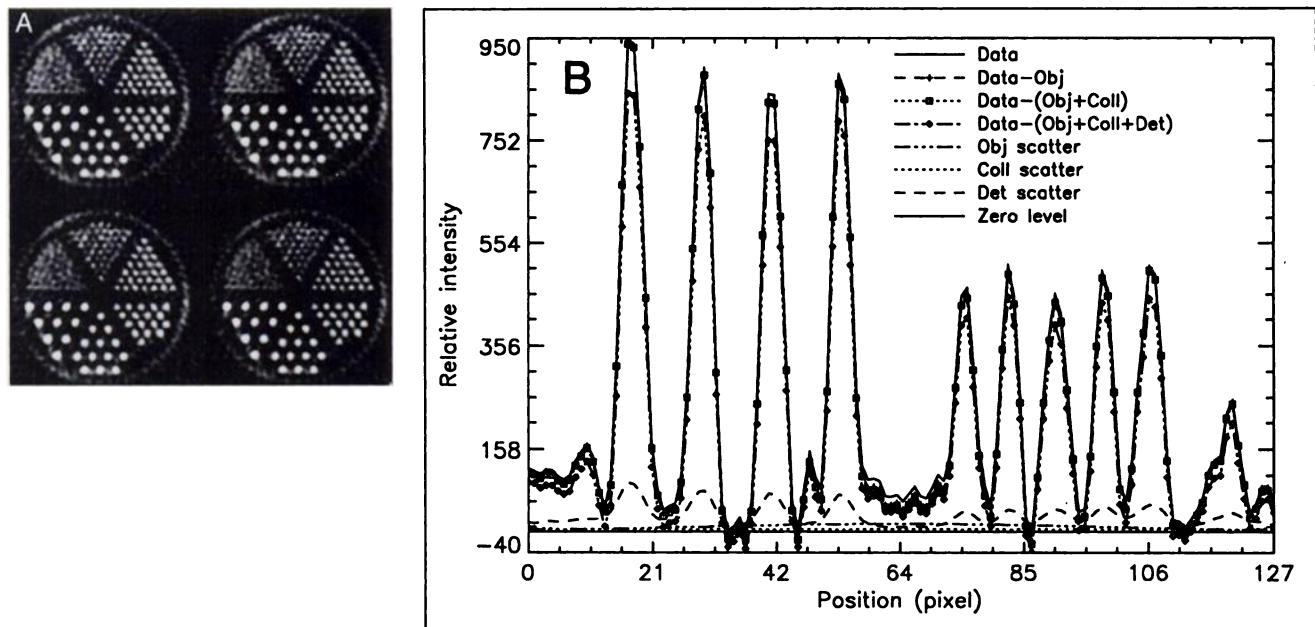


FIGURE 15. (A) Image of the pie hot spot phantom. Clockwise: without correction; object scatter subtracted; object and collimator scatter subtracted; object, collimator and detector scatter subtracted. (B) Profiles through hot spots showing the scatter contributions and the resultant profiles after the successive corrections.

TABLE 3
FWHM and FWTM of the Response Function to a Line Source of ^{22}Na at the Center of the Cylindrical Phantom

	Uncorrected	Object	Collimator	Detector
FWHM (mm)	2.2	2.2	2.2	2.1
FWTM (mm)	4.8	4.8	4.8	4.7

The images of the line source were reconstructed using a ramp filter of cut-off frequency 2.7 cm^{-1} . The source had an effective diameter of 0.85 mm.

collimator and the detector components as object size changes.

The image contrast was evaluated from the cold spot images of Figure 14A according to the definition of Equation 11. Relatively large ROIs were used in the hot and cold regions to avoid statistical and resolution effects on contrast estimation. The estimated values for uncorrected and corrected images are given in Table 2. Removal of object scatter produces the most significant contrast enhancement, in accordance with what many authors have shown (2–6). Once again, removal of either collimator or detector scatter does not produce significant contrast enhancement.

Resolution Recovery. Figure 15A displays the uncorrected pie hot spot image and the successively corrected images for the three scatter components. It is evident that the image corrected for all three components is superior to the others. Figure 15B shows the profiles of the uncorrected and corrected images. The object and collimator scatter components are fairly uniform and, therefore, their intensities do not follow the intensity of the source in the object. This phenomenon has been observed by other workers (3–5). Since the collimator scatter contribution in images is weak and broadly distributed, its inclusion in the object scatter component for correction would have negligible effect on the quality of corrected images.

The detector scatter contribution follows the source activity more closely, in accordance with what we observe in the projection fits where the detector scatter has a narrow distribution wrapping up the geometric component (see Figs. 7 and 8). Subtraction of the detector scatter component leads to slight improvements in edge sharpness, which can be noticed from the smaller structure in the profile of Figure 15B. This is also observed from the resolution measured on the reconstructed line source profiles (Table 3). However, subtraction of the detector scatter also removes substantial amounts of rather well-positioned events which can be considered useful for quantitation. It is therefore recommended that this component be restored and used in image reconstruction.

CONCLUSION

New methods to estimate object, collimator and detector nonstationary scatter response functions for high-resolution PET have been developed. The observations made

in this work lead to the following conclusions: first, subtraction of object scatter improves contrast and quantitative accuracy but has little effect on spatial resolution in a small animal PET system; second, the contribution from collimator scatter is small and similar in shape to the object scatter contribution, so it can be safely combined with the latter for correction; third, regardless of the slight resolution improvement, the overall effects of subtracting detector scatter is undesirable because it lowers the signal without improving image contrast. A complementary restoration model, capable of preserving the geometric component, removing object scatter, restoring detector scatter and suppressing noise generated by the scatter correction is thus needed in high-resolution PET. Work is now in progress to develop such a scatter correction model.

REFERENCES

1. Bentourkia M, Msaki P, Cadorette J, Héon M, Lecomte R. Assessment of scatter components in a very high-resolution PET scanner. *J Nucl Med* 1993;34:136P.
2. Barney JS, Rogers JG, Harrop R, Hoverath H. Object shape dependent scatter simulations for PET. *IEEE Trans Nucl Sci* 1991;38:719–725.
3. Bergström M, Eriksson L, Bohm C, Blomqvist G, Litton J. Correction for scattered radiation in a ring detector positron camera by integral transformation of the projections. *J Comp Assist Tomogr* 1983;7:42–50.
4. Hoverath H, Kuebler WK, Ostertag HJ, et al. Scatter correction in the transaxial slices of a whole-body positron emission tomograph. *Phys Med Biol* 1993;38:717–728.
5. Prati P, Lanza P, Corvisiero P, Guzzardi R, Sorace O. Verification of the integral transformation of the projections technique for scatter correction in positron tomographs. *Eur J Nucl Med* 1993;20:255–259.
6. Shao L, Karp JS. Cross-plane scattering correction: point source deconvolution in PET. *IEEE Trans Med Imag* 1991;10:234–239.
7. Thompson CJ. The effect of collimation on scatter fraction in multi-slice PET. *IEEE Trans Nucl Sci* 1988;35:598–602.
8. Derenzo SE, Huesman RH, Cahoon JL, et al. Initial results from the Donner 600 crystal positron tomograph. *IEEE Trans Nucl Sci* 1987;NS-34:321–325.
9. Derenzo SE, Huesman RH, Cahoon JL, et al. A positron tomograph with 600 BGO crystal and 2.6 mm resolution. *IEEE Trans Nucl Sci* 1988;35:659–664.
10. Hoffman EJ. Signal to noise improvement in PET using BGO. *Proc NATO ASI Phys Eng Med Imag* 1987;E119:874–881.
11. Lecomte R, Cadorette J, Jouan A, Héon M, Rouleau D, Gauthier G. High resolution positron emission tomography with a prototype camera based on solid state scintillation detectors. *IEEE Trans Nucl Sci* 1990;37:805–811.
12. Lecomte R, Martel C, Cadorette J. Study of the resolution performance of an array of discrete detectors with independent readouts for positron emission tomography. *IEEE Trans Med Imag* 1991;10:347–357.
13. Murthy K, Thompson CJ, Weinberg IN, Mako FM. Measurement of the coincidence response of very thin BGO crystals. *IEEE Trans Nucl Sci* 1994;41:1430–1435.
14. Acchiappati D, Cerullo N, Guzzardi R. Assessment of the scatter fraction evaluation methodology using Monte Carlo simulation techniques. *Eur J Nucl Med* 1989;15:683–686.
15. Bendriem B, Wong WH, Michel C, Adler S, Mullani N. Analysis of scatter deconvolution technique in PET using Monte Carlo simulation. *J Nucl Med* 1987;28:681.
16. Msaki P, Axelsson B, Dahl CM, Larsson SA. Generalized scatter correction method in SPECT using point scatter distribution functions. *J Nucl Med* 1987;28:1861–1869.
17. McKee BTA, Hogan MJ, Howse DCN. Compton scattering in a large-aperture positron imaging system. *IEEE Trans Med Imag* 1988;3:198–202.
18. Thompson CJ, Moreno-Cantu J, Picard Y. PETSIM: Monte Carlo simulation of all sensitivity and resolution parameters of cylindrical positron imaging systems. *Phys Med Biol* 1992;37:731–749.
19. Lecomte R, Cadorette J, Rodrigue S, et al. A PET camera with multispectral data acquisition capabilities. *IEEE Trans Nucl Sci* 1993;40:1067–1074.

20. Lecomte R, Martel C, Carrier C. Status of BGO-avalanche photodiode detectors for spectroscopy and timing measurements. *Nucl Instr Meth Phys Res* 1989;A278:585-597.
21. Lightstone AW, McIntyre RJ, Lecomte R, Schmitt D. A bismuth germanate-avalanche photodiode module designed for use in high resolution positron emission tomography. *IEEE Trans Nucl Sci* 1986;NS-33:456-459.
22. Bevington PR. *Data reduction and error analysis for the physical sciences*. New York, McGraw-Hill; 1969.

EDITORIAL

Scattered Photons as "Good Counts Gone Bad:" Are They Reformable or Should They Be Permanently Removed from Society?

In general, the quality of an image can be described (quantitatively) by its signal-to-noise ratio (I), which directly affects diagnostic and quantitative accuracy. The signal-to-noise ratio describes the relative "strength" of the desired information and the noise (due to the statistics of radioactive decay, for example) in the image. The signal is typically thought of as the difference or contrast between a target and the surrounding activity. In practice, this contrast is provided in the patient by the radiotracer's distribution. The goal of the imaging system is to preserve this contrast in the image. Contrast is maintained by avoiding blurring, which smears counts from higher-activity regions into lower-activity regions (and vice versa), thus reducing image contrast. Therefore, spatial resolution, in its broadest sense, and contrast are closely linked. This relationship is quantitatively described by the imaging system's modulation transfer function, which is the Fourier transform of the point spread function. While the modulation transfer function is obtained from a conventional measure of spatial resolution, it is actually the ratio of the contrast in the image to that in the object as a function of spatial frequency (2). Inclusion of scattered photons in the image reduces contrast; this is partially reflected in a change in the point spread function and modula-

tion transfer function (2). The amount of scatter depends on the distribution of activity within the patient, the patient's body habitus, the imaging geometry of the system, the system's energy resolution and the pulse height window setting.

The design of a PET or SPECT system must address these issues by attempting to simultaneously maximize spatial resolution and sensitivity, while minimizing the acceptance of scattered photons. In practice, these competing design goals lead to an "optimum" (in the designer's mind) compromise, and real-world scanners have less-than-ideal resolution, sensitivity, and scatter characteristics. There is, thus, much interest in software-based postacquisition approaches to these problems. For the sake of simplicity, many software approaches begin with the assumption of a linear, shift-invariant system. Such a system responds linearly to changes in activity distribution regardless of the position of the activity within the field of view. In such a situation, the measured projection data can be considered as the convolution of the object with the imaging system's response:

$$p = o * h, \quad \text{Eq. 1}$$

where p represents the projection data, o the object and h the imaging system's response (i.e., the point spread function). The asterisk represents convolution. It is important to note that h contains both resolution and scatter effects. The convolution theorem states that convolution in real space is equivalent to multiplication in Fourier space. If we use capital letters

to denote the Fourier transform of a function, the above equation thus becomes:

$$P = O H. \quad \text{Eq. 2}$$

In such a situation, o can be obtained from p by deconvolution with a known h (i.e., based on a measurement of a point source). Deconvolution is usually performed in Fourier space, where mathematically it is a simple division:

$$O = P/H, \quad \text{Eq. 3}$$

in which o is obtained from O by taking the inverse Fourier transform. H^{-1} is known as the inverse filter. In the absence of noise, such a filter will perfectly restore a blurred projection. In practice, the use of such a filter would lead to unacceptably large noise amplification, and a combination of inverse filtering and low-pass filtering must be used. This approach forms the basis for all Fourier-based restoration filtering (e.g., Wiener or Metz filtering) in nuclear medicine. Such filters usually are composed of an inverse component (i.e., a boost) at low to intermediate spatial frequencies, followed by a roll-off (i.e., a cut) at intermediate to high spatial frequencies. Since scatter is mainly though by no means exclusively a low spatial frequency phenomenon, I have previously argued that the main effect of such filtering is scatter reduction, by the equivalent of deconvolution. Of importance, deconvolution here reduces scatter through a process of repositioning of scattered events, not by their elimination (3,4).

Received Aug. 25, 1994; accepted Oct. 5, 1994.
For correspondence or reprints contact: Jonathan Links, PhD, Dept. of Radiation Health Sciences and Environmental Health Sciences, Johns Hopkins Medical Institute, 615 N. Wolfe St., Baltimore, MD 21205-2179.